Implicit WENO Scheme and High Order Viscous Formulas for Compressible Flows

Yiqing Shen[*], Baoyuan Wang[†], Gecheng Zha[‡]

Dept. of Mechanical and Aerospace Engineering
University of Miami
Coral Gables, Florida 33124
E-mail: yqshen@miami.edu, gzha@miami.edu

Abstract

The purpose of this paper is to develop a robust and efficient high order fully conservative finite difference scheme for compressible Navier-Stokes equations. The 5th order WENO scheme is used for the inviscid fluxes. A conservative fourth order accuracy finite central differencing scheme is developed for the viscous terms. An improved ε value of 10^{-2} is suggested for the WENO smooth factors calculation, which removes the weight oscillation and significantly improves the convergence rate and level. The wall surface is taken as half-point mesh so that the no slip wall boundary condition can be accurately imposed. A 3th order accurate finite difference scheme is given to treat wall boundary condition. The implicit time marching method with unfactored Gauss-Seidel line relaxation is used with the high order scheme to achieve steady state solutions with high convergence rate.

1   Introduction

Since the application of computational fluid dynamics becomes more and more popular, the demand on high accuracy and high efficiency CFD solutions also becomes stronger to satisfy the needs of the broad engineering problems. So far, most of the engineering applications employ the 2nd order numerical accuracy. The high order schemes (higher than 3rd order) are mostly limited to the fundamental research such as high fidelity turbulence simulation (e.g. Large Eddy Simulations and Direct Numerical Simulation) and aeroacoustic calculation. The reason is that the high order schemes are generally not mature enough for robust engineering applications.

For aerospace engineering applications with shock waves or contact surfaces, the essentially non-oscillatory (ENO) or weighted essentially non-oscillatory (WENO) schemes are attractive for their capability to treat the discontinuities and achieve the consistent high order accuracy in the smooth regions. By using a convex combination of all candidate stencils to replace the smoothest one in the ENO scheme, the WENO scheme has more advantages over its ENO counterpart. For example, it approaches certain optimal accuracy in smooth regions and has better convergence rate due to the smoother numerical flux used. From its appearance [1, 2] to present, the WENO schemes have been extensively applied to different flow problems in many areas.

Titarev and Toro [3] firstly carried out an extension of the finite-volume WENO schemes to three space dimensions with higher orders of accuracy. Although the finite volume WENO schemes can be

---

[*]   Research Scientist, AIAA Member
[†]   Ph.D. Candidate
[‡]   Associate Professor, AIAA Member

applied on more general unstructured meshes, they need higher computational cost than the WENO finite difference scheme. As pointed out in references [3, 4], when the piece-wise parabolic reconstruction is used in two space dimensions, the finite volume WENO schemes require approximately three times more CPU time than the corresponding finite difference WENO schemes. In three space dimensions, the difference is about nine times. Hence, for the structured meshes, the finite difference WENO schemes are preferable. In [5, 6, 7], the formally high-order accurate WENO shock-capturing method using a third-order total-variation diminishing (TVD) Runge-Kutta time evolution scheme is applied to the reshocked two-dimensional single-mode Richtmyer-Meshkov instability[5], the shallow water and the open-channel flow equations[6], and to study adaptive mesh refinement techniques for multi-dimensional hydrodynamic simulation[7]. Sjogreen and Yee [8] used the low dissipation sixth-order spatial and fifth-order WENO schemes with the standard fourth-order Runge-Kutta method to study the supersonic reactive flows, even for 2-D problem.

In the standard WENO scheme, a Riemann solver is needed to capture the discontinuities. There are two ways to evaluate the Riemann solver fluxes. For the WENO finite difference scheme, Shu suggested that the WENO reconstruction be directly applied to the split fluxes from left or right[9]. For the WENO finite volume method, the WENO reconstruction can be applied to the conservative variables, which are then used to evaluate the Riemann fluxes[9] in the same manner as the MUSCL method of Van Leer for the TVD schemes[10]. The WENO finite difference methods is more efficient than the finite volume method in multi-dimensional calculation due to avoiding the Gaussian integrals.

Chen et al [11] presented a class of implicit WENO schemes for the incompressible Navier-Stokes equations, in which the lower-upper symmetric Gauss-Seidel (LU-SGS) relaxation is used for computing steady state solutions. Yang et al [12] have extended this method to the resolution of steady compressible Navier-Stokes equations. Cadiou and Tenaud[13] proposed an implicit WENO shock capturing scheme for unsteady flows and applied it to one-dimensional Euler equations. The use of WENO spatial operator not only enhances the accuracy of solutions, but also improves the convergence rate for the steady state computation as compared with using the ENO counterpart. In references [14, 15], it is found that LU-SGS is less efficient than Gauss-Seidel line relaxation method for the steady state solution computation.

Even though the finite difference WENO scheme given by Shu et al.[9, 2]is conservative, how to achieve the high order conservative finite central differencing scheme for the viscous derivatives of compressible Navier-Stokes equations is not well addressed in the CFD community.

The purpose of this paper is to develop a robust and efficient high order finite difference scheme for compressible Navier-Stokes equations. The WENO scheme of Jiang and Shu [2] is modified for inviscid fluxes and a fully conservative fourth-order accurate central finite differencing scheme is proposed for viscous fluxes. The following numerical techniques are developed in this paper to achieve the aforementioned purpose: 1) In the cases with the shock waves, the weights of WENO may oscillate and result in low convergence rate and low convergence level. However, the oscillation can be depressed by reasonably amplifying the parameter ε introduced in the weights so that the high convergence rate and level are obtained. 2) A conservative fourth order accuracy finite central differencing scheme is proposed for the viscous terms of compressible Navier-stokes equations, where 4th order central differencing scheme are constructed with the stencil width not wider than the WENO stencil width. 3) The wall surface is taken as half-point mesh so that the no slip wall boundary condition can be accurately imposed in a conservative manner. A 3th order accuracy finite difference scheme is given to treat the first mesh node on the wall. 4) The implicit time marching method with unfactored Gauss-Seidel line relaxation is used with the high order WENO scheme to achieve steady state solutions with high convergence rate.

2   The Numerical Method

2.1   Governing Equations

The normalized Navier-Stokes equations governing compressible viscous flows can be written in the Cartesian coordinate as:

$$\frac{\partial Q}{\partial t} + \frac{\partial E}{\partial x} + \frac{\partial F}{\partial y} + \frac{\partial G}{\partial z} = \frac{1}{Re}\left(\frac{\partial R}{\partial x} + \frac{\partial S}{\partial y} + \frac{\partial T}{\partial z}\right) \tag{1}$$

$$
Q = \begin{bmatrix} \rho \\ \rho u \\ \rho v \\ \rho w \\ \rho e \end{bmatrix},\;
E = \begin{bmatrix} \rho u \\ \rho u^2 + p \\ \rho uv \\ \rho uw \\ (\rho e + p)u \end{bmatrix},\;
F = \begin{bmatrix} \rho v \\ \rho uv \\ \rho v^2 + p \\ \rho vw \\ (\rho e + p)v \end{bmatrix},\;
G = \begin{bmatrix} \rho w \\ \rho uw \\ \rho vw \\ \rho w^2 + p \\ (\rho e + p)w \end{bmatrix},
$$

$$
R = \begin{bmatrix} 0 \\ \tau_{xx} \\ \tau_{xy} \\ \tau_{xz} \\ u_k\tau_{xk} - q_x \end{bmatrix},\;
S = \begin{bmatrix} 0 \\ \tau_{xy} \\ \tau_{yy} \\ \tau_{yz} \\ u_k\tau_{yk} - q_y \end{bmatrix},\;
T = \begin{bmatrix} 0 \\ \tau_{xz} \\ \tau_{yz} \\ \tau_{zz} \\ u_k\tau_{zk} - q_z \end{bmatrix},
$$

The repeated index k stands for the Einstein summation over x,y and z. The stress τ and heat flux q are,

$$\tau_{ik} = \mu\left[(\frac{\partial u_i}{\partial x_k} + \frac{\partial u_k}{\partial x_i}) - \frac{2}{3}\delta_{ik}\frac{\partial u_j}{\partial x_j}\right]$$

$$q_j = \frac{-\mu}{(\gamma - 1)M_\infty^2 Pr}\frac{\partial T}{\partial x_j}$$

The equation of state is

$$\rho e = \frac{p}{\gamma - 1} + \frac{1}{2}\rho(u^2 + v^2 + w^2)$$

In the generalized coordinates, Eq.(1) can be written as:

$$\frac{\partial Q'}{\partial t} + \frac{\partial E'}{\partial \xi} + \frac{\partial F'}{\partial \eta} + \frac{\partial G'}{\partial \zeta} = \frac{1}{Re}\left(\frac{\partial R'}{\partial \xi} + \frac{\partial S'}{\partial \eta} + \frac{\partial T'}{\partial \zeta}\right) \tag{2}$$

where,

$$Q' = \frac{1}{J}Q,$$

$$E' = \frac{1}{J}(\xi_t U + \xi_x E + \xi_y F + \xi_z G),$$

$$F' = \frac{1}{J}(\eta_t U + \eta_x E + \eta_y F + \eta_z G),$$

$$G' = \frac{1}{J}(\zeta_t U + \zeta_x E + \zeta_y F + \zeta_z G),$$

$$R' = \frac{1}{J}(\xi_x R + \xi_y S + \xi_z T),$$

$$S' = \frac{1}{J}(\eta_x R + \eta_y S + \eta_z T),$$

$$T' = \frac{1}{J}(\zeta_x R + \zeta_y S + \zeta_z T).$$

For simplicity, the prime $\prime$ in Eq.(2) will be omitted.

In the above equations, ρ is the density, $u, v,$ and w are the Cartesian velocity components in x, y and z directions, p is the static pressure, and e is the total energy per unit mass, μ is the molecular viscosity, J is the transformation Jacobian, γ, Re, M_∞ and Pr are the ratio of specific heat, Reynolds number, freestream Mach number and Prandtl number, respectively. Eqs.(2) are discretized into an implicit form as

$$\frac{1}{J\Delta t}\Delta Q^{n+1} + (E_{i+\frac{1}{2}}^{n+1} - E_{i-\frac{1}{2}}^{n+1}) + (F_{j+\frac{1}{2}}^{n+1} - F_{j-\frac{1}{2}}^{n+1}) + (G_{k+\frac{1}{2}}^{n+1} - G_{k-\frac{1}{2}}^{n+1}) = \frac{1}{Re}[(\tilde{R}_{i+\frac{1}{2}}^{n+1} - \tilde{R}_{i-\frac{1}{2}}^{n+1}) + (\tilde{S}_{j+\frac{1}{2}}^{n+1} - \tilde{S}_{j-\frac{1}{2}}^{n+1}) + (\tilde{T}_{k+\frac{1}{2}}^{n+1} - \tilde{T}_{k-\frac{1}{2}}^{n+1})] \tag{3}$$

where, the inviscid numerical fluxes $E_{i+\frac{1}{2}}^{n+1}$, $F_{j+\frac{1}{2}}^{n+1}$ and $G_{k+\frac{1}{2}}^{n+1}$ are evaluated by WENO scheme with a Riemann solver as described in Section 2.2-2.3, and the viscous numerical fluxes $\tilde{R}_{i+\frac{1}{2}}^{n+1}$, $\tilde{S}_{j+\frac{1}{2}}^{n+1}$ and $\tilde{T}_{k+\frac{1}{2}}^{n+1}$ are evaluated by high order central differencing as described in Section 2.4.

2.2 Flux Difference Splitting

The Roe's [16] flux difference scheme is used as the Riemann solver with the WENO scheme in this paper. For the rest of the paper we will take the flux in ξ direction as the example to explain the numerical methods. Other directions can be obtained following the symmetric rule. The flux $E(Q)$ is a homogeneous function of degree one, i.e.,

$$E = A \cdot Q, \tag{4}$$

where A is the jacobian

$$A = \frac{\partial E}{\partial Q}.$$

For the Roe scheme,

$$E_{i+\frac{1}{2}} = \frac{1}{2}[E(Q^L) + E(Q^R) - \tilde{A}(Q^R - Q^L)]_{i+\frac{1}{2}} \tag{5}$$

The high order accuracy of $E_{i+1/2}$ is determined by achieving the high order accuracy of the left and right conservative variables Q^L and Q^R in the same way as the MUSCL scheme suggested by van Leer[10].

2.3 WENO Scheme[2]

The the finite difference 5th-order accuracy WENO scheme suggested by Jiang and Shu [2] is used to evaluate the conservative variables Q^L and Q^R. The WENO scheme scheme for a variable u^L can be written as:

$$u_{i+1/2}^L = \omega_0 q_0 + \omega_1 q_1 + \omega_2 q_2$$

where

$$q_0 = \frac{1}{3}u_{i-2} - \frac{7}{6}u_{i-1} + \frac{11}{6}u_i$$

$$q_1 = -\frac{1}{6}u_{i-1} + \frac{5}{6}u_i + \frac{1}{3}u_{i+1}$$

$$q_2 = \frac{1}{3}u_i + \frac{5}{6}u_{i+1} - \frac{1}{6}u_{i+2}$$

and

$$\omega_k = \frac{\alpha_k}{\alpha_0 + \cdots + \alpha_{r-1}},$$

$$\alpha_k = \frac{C_k}{(\varepsilon + IS_k)^p}, \quad k = 0, \cdots, r-1 \tag{6}$$

$$C_0 = 0.1, \quad C_1 = 0.6, \quad C_2 = 0.3$$

$$IS_0 = \frac{13}{12}(u_{i-2} - 2u_{i-1} + u_i)^2 + \frac{1}{4}(u_{i-2} - 4u_{i-1} + 3u_i)^2$$

$$IS_1 = \frac{13}{12}(u_{i-1} - 2u_i + u_{i+1})^2 + \frac{1}{4}(u_{i-1} - 4u_i + 3u_{i+1})^2$$

$$IS_2 = \frac{13}{12}(u_i - 2u_{i+1} + u_{i+2})^2 + \frac{1}{4}(u_i - 4u_{i+1} + 3u_{i+2})^2$$

where, ε is introduced to avoid the denominator becoming zero. Jiang ans Shu's numerical tests indicate that the results are not sensitive to the choice of ε, as long as it is in the range of 10^{-5} to 10^{-7}. In their paper[2], ε is taken as 10^{-6}.

In our numerical experiments, it is observed that when there are shock waves in the flow fields, the weights of the WENO scheme may oscillate. The convergence of the numerical solutions are affected seriously. These can be seen from the numerical examples in section 3.5 and 3.6. In this paper, the parameter ε is taken as $\varepsilon = 10^{-2}$, which significantly improves the convergence rate and convergence level.

The u^R is constructed symmetrically as u^L about $i + 1/2$.

2.4 The Discretization of Viscous Terms

A fully conservative fourth-order accurate finite central differencing scheme for the viscous terms is suggested in this paper. These central differencing scheme are constructed to how the stencil width within the stencil width of the WENO scheme. We take the viscous flux derivative in ξ-direction as the example.

$$\frac{\partial R}{\partial \xi}\Big|_i = \tilde{R}_{i+1/2} - \tilde{R}_{i-1/2} \tag{7}$$

where

$$\tilde{R}_{i-1/2} = \frac{1}{24\Delta\xi}(-R_{i+1/2} + 26R_{i-1/2} - R_{i-3/2}) \tag{8}$$

$$R_{i-1/2} = [(\xi_x \tau_{xx}) + (\eta_y \tau_{xy}) + (\zeta_z \tau_{xz})]_{i-1/2}$$

$$(\tau_{xx})_{i-1/2} = \mu|_{i-1/2}\{\frac{4}{3}\left[(\xi_x \frac{\partial u}{\partial \xi})|_{i-1/2} + (\eta_x \frac{\partial u}{\partial \eta})|_{i-1/2} + (\zeta_x \frac{\partial u}{\partial \zeta})|_{i-1/2}\right] - \frac{2}{3}[(\xi_y \frac{\partial v}{\partial \xi})|_{i-1/2} + (\eta_y \frac{\partial v}{\partial \eta})|_{i-1/2} + (\zeta_y \frac{\partial v}{\partial \zeta})|_{i-1/2} (\xi_z \frac{\partial w}{\partial \xi})|_{i-1/2} + (\eta_z \frac{\partial w}{\partial \eta})|_{i-1/2} + (\zeta_z \frac{\partial w}{\partial \zeta})|_{i-1/2}]\} \tag{9}$$

If R in Eq.(8) can be approximated with the accuracy order not lower than 4th order, the Taylor expansion analysis of (7) and (8) will give

$$\tilde{R}_{i+1/2} - \tilde{R}_{i-1/2} = R'(\xi_i) + O(\Delta\xi^4)$$

Where the 4th order accuracy is achieved. It needs to point out that in Eq.(7), $\tilde{R}_{i+1/2}$ can not be replaced by $R_{i+1/2}$. Otherwise, the 4th order accuracy can not be achieved even though the high order approximation of $R_{i+1/2}$ is used.

5

In order to achieve the highest order accuracy of R_I $(I = i - 3/2, i - 1/2, i + 1/2)$ in a least stencil not wider than the total width of the WENO stencils, for example, the stencil $S = (x_{i+r}, x_{i+r+1}, \cdots, x_{i+s})$ for all $\frac{\partial u}{\partial \eta}|_I$, $I = i - 3/2, i - 1/2, i + 1/2$, we give the following formulas,

$$\mu_I = \sum_{l=m}^{n} C_l^I \mu_{i+l}, \ m = -2, n = 1, \tag{10}$$

$$\frac{\partial u}{\partial \xi}|_I = \frac{1}{\Delta \xi} \sum_{l=r}^{s} D_l^I u_{i+l}, \ r = -3, s = 2, \tag{11}$$

$$\frac{\partial u}{\partial \eta}|_I = \sum_{l=m}^{n} C_l^I \frac{\partial u}{\partial \eta}|_{i+l,j}, \ m = -2, n = 1, \tag{12}$$

where

$$\frac{\partial u}{\partial \eta}|_{i,j} = \frac{1}{\Delta \eta} \sum_{l=p}^{q} C_l^c u_{i,j+l}, \ p = -2, q = 2, \tag{13}$$

The other terms are determined similarly.

By choosing different ranges for $(m, n), (r, s), (p, q)$ and different coefficients C_l^I, D_l^I, C_l^c, one can obtain the different order accuracy of the viscous terms.

One principle of choosing $(m, n), (r, s), (p, q)$ is to ensure the approximation of $\frac{\partial R}{\partial \xi}|_i$ (Eq.(7))is a central differencing. In this paper, we take $(m, n) = (-2, 1), (r, s) = (-3, 2), and \ (p, q) = (-2, 2)$, and the coefficients C_l^I, D_l^I, C_l^c are given in Tables 1-3.

Taylor expansion analysis of (10)-(13) show that $\mu_I, \frac{\partial u}{\partial \eta}|_I, \frac{\partial u}{\partial \eta}|_{i,j}$ achieve fourth-order accuracy, and $\frac{\partial u}{\partial \xi}|_I$ achieve fifth-order accuracy.

Table 1: The coefficients of C_l^I

I	C_{-2}^I	C_{-1}^I	C_0^I	C_1^I
$i - 3/2$	5/16	15/16	-5/16	1/16
$i - 1/2$	-1/16	9/16	9/16	-1/16
$i + 1/2$	1/16	-5/16	15/16	5/16

Table 2: The coefficients of D_l^I

I	D_{-3}^I	D_{-2}^I	D_{-1}^I	D_0^I	D_1^I	D_2^I
$i - 3/2$	71/1920	-141/128	69/64	1/192	-3/128	3/640
$i - 1/2$	-3/640	25/384	-75/64	75/64	-25/384	3/640
$i + 1/2$	-3/640	3/128	-1/192	-69/64	141/128	-71/1920

Table 3: The coefficients of C_l^c

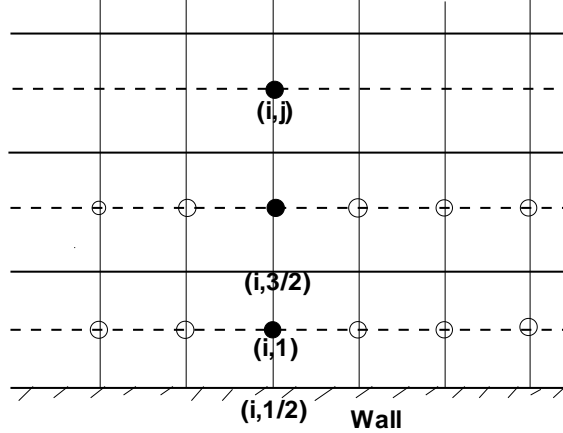| C_{-2}^c	C_{-1}^c	C_0^c	C_1^c	C_2^c
1/12	-8/12	0	8/12	-1/12

Figure 1: Sketch of the computational grid

2.5 Wall Boundary Treatment

Since the numerical strategy is to achieve a fully conservative finite differencing scheme, the solution point near the wall boundary is not located on the wall surface as the conventional finite difference scheme. Instead, the solution point is located half mesh interval away from the wall as illustrated in Fig.1. For example, to calculate $\frac{\partial F}{\partial \eta}$ at point $(i, 1)$,

$$\frac{\partial F}{\partial \eta} = \frac{F_{i,3/2} - F_{i,1/2}}{\Delta \eta},$$

For the flux $F_{1/2}$ on the wall, we have

$$F_{\frac{1}{2}} = \begin{bmatrix} \rho v|_w \\ \rho uv|_w \\ \rho v^2 + p|_w \\ \rho vw|_w \\ (\rho e + p)v|_w \end{bmatrix} = \begin{bmatrix} 0 \\ 0 \\ p|_w \\ 0 \\ 0 \end{bmatrix}$$

In this study, the third-order reconstruction is used for p_w,

$$p_w = \frac{1}{6}(11p_1 - 7p_2 + 2p_3)$$

and the third-order reconstruction for $Q_{i,3/2}^L$ and $Q_{i,3/2}^R$ are used for the interface 3/2,

$$Q_{i,3/2}^L = \frac{1}{6}(2Q_1 + 5Q_2 - Q_3), \quad Q_{i,3/2}^R = \frac{1}{6}(11Q_2 - 7Q_3 + 2Q_4)$$

2.6 The Time Discretization

For the one-dimensional unsteady problems presented in this paper, the high-order Runge-Kutta methods are used. The governing equations can be written as an ordinary differential equations form:

$$\frac{du}{dt} = L(u),$$

7

where $L(u)$ is the spatial term. The fourth-order Runge-Kutta scheme [17] is expressed as

$$u^{(1)} = u^n + \frac{1}{2}\Delta t L(u^n)$$

$$u^{(2)} = u^n + \frac{1}{2}\Delta t L(u^{(1)})$$

$$u^{(3)} = u^n + \Delta t L(u^{(2)})$$

$$u^{(n+1)} = \frac{1}{3}[-u^n + u^{(2)} + 2u^{(2)} + u^{(3)}] + \frac{1}{6}\Delta t L(u^{(3)})]$$

For multi-dimensional problems, the implicit Gauss-Seidel line relaxation with two alternative direction sweeps in each time step is applied. We expand each term in Eq.(5) in Taylor's series about interface $i+1/2$,

$$E^L_{i+1/2}|^{n+1} = E^L_{i+1/2}|^n + (\frac{\partial E}{\partial U}|^L_{i+1/2})|^n \Delta U^L_{i+1/2}|^{n+1} + O(\Delta t^2)$$

$$= E^L_{i+1/2}|^n + A^L_{i+\frac{1}{2}}|^n \Delta U^L_{i+1/2}|^{n+1} + O(\Delta \xi \Delta t) + O(\Delta t^2)$$

$$E^R_{i+1/2}|^{n+1} = E^R_{i+1/2}|^n + (\frac{\partial E}{\partial U}|^R_{i+1/2})|^n \Delta U^R_{i+1/2}|^{n+1} + O(\Delta t^2)$$

$$= E^R_{i+1/2}|^n + A^R_{i+\frac{1}{2}}|^n \Delta U^R_{i+1/2}|^{n+1} + O(\Delta \xi \Delta t) + O(\Delta t^2)$$

and,

$$\tilde{A}(U^R - U^L)|^{n+1}_{i+1/2} =$$

$$\tilde{A}(U^R - U^L)|^n_{i+1/2} + \tilde{A}_{i+1/2}|^n(\Delta U^R_{i+1/2}|^{n+1} - \Delta U^L_{i+1/2}|^{n+1}) + O(\Delta \xi \Delta t)$$

And the first-order approximation is used for the implicit terms to enhance the diagonal dominance,

$$\Delta U^L_{i+1/2}|^{n+1} = \Delta U^{n+1}_i, \quad \Delta U^R_{i+1/2}|^{n+1} = \Delta U^{n+1}_{i+1},$$

the same methods are applied for fluxes F and G, R,S and T. We then obtain the final implicit form as following,

$$\bar{B}\Delta U^{n+1}_{i,j,k} + A^+\Delta U^{n+1}_{i+1,j,k} + A^-\Delta U^{n+1}_{i-1,j,k} + B^+\Delta U^{n+1}_{i,j+1,k} + B^-\Delta U^{n+1}_{i,j-1,k} +$$

$$C^+\Delta U^{n+1}_{i,j,k+1} + C^-\Delta U^{n+1}_{i,j,k-1} = RHS^n \tag{14}$$

The Gauss-Seidel line iteration in a certain sweep direction, for example, in ξ direction assuming the sweeping from small index value to large value, can be written as

$$B^-\Delta U^{n+1}_{i,j-1,k} + \bar{B}\Delta U^{n+1}_{i,j,k} + B^+\Delta U^{n+1}_{i,j+1,k} = RHS' \tag{15}$$

where,

$$RHS' = RHS^n - A^+\Delta U^n_{i+1,j,k} - A^-\Delta U^{n+1}_{i-1,j,k} - C^+\Delta U^n_{i,j,k+1} - C^-\Delta U^{n+1}_{i,j,k-1} \tag{16}$$

The accuracy of the converged solution is controlled by RHS, which is calculated by the high order WENO and central differencing described in section 2.2-2.5.

3 Results and Discussion

3.1 The Sod Problem

The governing equation is one-dimensional Euler equations,

$$\frac{\partial U}{\partial t} + \frac{\partial F}{\partial x} = 0 \tag{17}$$

where $U = (\rho, \rho u, \rho e)^T$, $F = (\rho u, \rho u^2 + p, u(\rho e + p))^T$, $p = (\gamma - 1)(\rho e - \rho u^2/2)$, $\gamma = 1.4$.

The initial solution is at rest with a diaphragm located in the the middle of the shock tube. The pressure on the left side of the diaphragm is 10 times higher than the pressure on the right side. At time level t=0, the diaphragm breaks. A shock wave propagates to the right side of the tube. A contact surface follows the shock tube traveling toward the right side at a lower speed. An expansion wave propagates to the left side of the tube.

Fig.2 is the temperature distribution, which shows that the 5th-order WENO reconstruction achieves better resolution of expansion wave than the 3rd-order one, but they have little difference for the shock wave profiles.

3.2 The Shu-Osher Problem

This test case is taken from Ref.[17]. The initial condition is

$$(\rho, u, p) = \begin{cases} (3.857143, 2.629369, 10.3333), & x < -4, \\ (1 + \varepsilon sin(5x), 0, 1), & x \geq -4. \end{cases}$$

It represents a Mach 3 shock wave interacting with a sine entropy wave. Fig.3 is the comparison of the density of the fifth-order WENO and the third-order WENO. It can be seen the high-order reconstruction obtains much better resolution of the smooth solution with complex structure.

3.3 Wall Boundary Layer

A laminar supersonic boundary layer flow on an adiabatic flat plate is employed to test the convergence rate. The incoming Mach number is 2.0. The Reynolds number based on the length of the flat plate is 4.0×10^4. The Prandtl number of 1.0 is used in order to compare with the analytical solution. The mesh size is 180×60.

Fig.4 shows that the maximum and $L2$ residuals can be converged to machine zero. The comparisons of velocity and temperature profiles of 5th-WENO and 3rd-order MUSCL reconstruction are shown in Figs.5-6. It shows that both reconstruction methods agree excellently with the Blasius solution.

3.4 Subsonic Flat Plate Turbulent Boundary Layer

The subsonic flat plate turbulent boundary layer is used as the second 2-D test example. In this case, the Baldwin-Lomax turbulence model is applied. The cell size is 80×60. The non-dimensional distance y^+ of the first point to the wall is kept under 0.2. The inlet Mach number is 0.5, and the Reynolds number is 4×10^6 based on the plate length. The flow is subsonic at inlet and outlet.

Similar as the laminar supersonic boundary layer flow, the residuals also can be converged to machine zero of 10^{-15}(See Figs.7). The comparisons from Fig.8 shows that the results of 5th-order WENO re-

9

construction is better than those of 3rd-order MUSCL reconstruction in the outer part of the law of the wall.

3.5 Transonic Converging-Diverging Nozzle

To examine the performance of the methodology in two-dimensional flow and the capability to capture the shock waves that do not align with the mesh lines, an inviscid transonic converging-diverging nozzle is calculated. The nozzle was designed and tested at NASA and was named as Nozzle A1[18]. The cell size is 175×80. The grid is clustered near the wall. The inlet Mach number is 0.22.

For this case, we studied the effects of different ε values in the weights of Eq.(6). Fig.9 gives the variations of weights vs iteration number in ξ-direction (interface $i + \frac{1}{2}$ at the point $(8.315, 1.117)$) between two shock waves with $\varepsilon = 10^{-6}$. It can be found that when the shock is formed at iteration number about 750, the weights begin to oscillate. ω_0 in the three conservative variables $\rho_{i+1/2}^L$, $(\rho u_{i+1/2}^L)$, and $(\rho v)_{i+1/2}^L$ approach to zero. Fig.9a shows that ω_1 and ω_2 in $\rho_{i+1/2}^L$ oscillate about the value of 0.5. Fig.9b shows ω_1 oscillate about the optimal weights 0.6, but ω_2 oscillate about 0.4. Fig.9c shows the similar behavior as Fig.9b, except with the larger amplitude.

Fig.10 gives the variations of weights vs iteration number in ξ-direction (interface $i + \frac{1}{2}$ at the point $(8.315, 1.117)$) with $\varepsilon = 10^{-2}$. We can see that after the oscillation occurs at iteration number 750 when the shock is formed, the weights ω_0, ω_1 and ω_2 return back to the optimal weights 0.1, 0.6 and 0.3, respectively. This behavior is very important to achieve high order accuracy in the smooth region.

Fig.11 shows that the residuals with $\varepsilon = 10^{-2}$ can converge to machine zero, whereas the residuals with $\varepsilon = 10^{-6}$ fluctuates at about the level of 10^{-2} and 10^{-4}, respectively.

Figs.13 and 14 give the comparison of pressure contours with $\varepsilon = 10^{-2}$ and $\varepsilon = 10^{-6}$. The converged solution with $\varepsilon = 10^{-2}$ is smoother than that with $\varepsilon = 10^{-6}$.

The Fig.12 shows the comparison of the pressure coefficients at the upper wall. The solution of $\varepsilon = 10^{-6}$ is more smeared for the shock profiles even though both capture the shock location well.

3.6 Transonic RAE2822 Airfoil

The steady state solution of the transonic RAE2822 airfoil is calculated using the Reynolds averaged Navier-Stokes equations with the Baldwin-Lomax turbulent model. The mesh size is 128×50, $M_\infty = 0.729$, $Re = 6.5 \times 10^6$, the angle of attack is $\theta = 2.31^o$.

Similar as in section 3.5, we take a point $(x, y) = (0.209, 0.066)$ under the airfoil and near the leading to investigate the variations of the weights of WENO-5.

Fig.15 gives the variations of weights vs iteration number in η-direction (interface $j + \frac{1}{2}$ at the point $(0.209, 0.066)$ with $\varepsilon = 10^{-6}$. It can be seen that the weights oscillate dramatically before about 400 iteration step. Then, they become basically stable. However, the weights do not approach their optimal values ($C_0 = 0.1, C_1 = 0.6$ and $C_2 = 0.3$). Instead, they approach the following values: $\omega_0 \to 0.05$, $\omega_1 \to 0.3$, and $\omega_0 \to 0.645$. Furthermore, from the zoomed plots (Fig.17), it can be seen that the weights are oscillating with small amplitude when $\varepsilon = 10^{-6}$.

Fig.16 shows the variations of weights vs iteration number in η-direction (interface $j + \frac{1}{2}$ at the point $(0.209, 0.066)$ with $\varepsilon = 10^{-2}$. It can be seen that after an initial oscillation with small amplitude, the weights approach to their optimal values ($C_0 = 0.1, C_1 = 0.6$ and $C_2 = 0.3$).

Figs.17a - 17b are the comparisons of ω_1 and ω_2, respectively. It can be seen that the weights with $\varepsilon = 10^{-2}$ are essentially constant, whereas the weights with $\varepsilon = 10^{-6}$ oscillate in the whole iteration process.

Again, from Fig. 18, we can see that the maximum residual and the L2 norm residual of $\varepsilon = 10^{-6}$ fluctuate about at the level of 10^{-2} and 10^{-5}, but the residuals of $\varepsilon = 10^{-2}$ can converge to machine zero.

Fig.19 is the comparison of the pressure coefficients with $\varepsilon = 10^{-6}$ and $\varepsilon = 10^{-2}$ at the airfoil surface. Both results with different ε values are in good agreement with the experiment, even though their convergence levels are very different as shown in fig.18.

Fig.20 shows the pressure contours of RAE2822 with $\varepsilon = 10^{-2}$. The overall flow field is smooth.

4   Conclusions

A robust and efficient high order fully conservative finite difference scheme is developed for Navier-Stokes equations. The study shows that the oscillation of the weights in high order WENO scheme can induce the low convergence rate and level. By using a reasonable amplified ε value in WENO scheme can overcome this drawback. A conservative fourth order accuracy finite central differencing scheme is developed for the viscous terms, which has the stencil width within the stencil of the WENO scheme. The implicit time marching method with unfactored Gauss-Seidel line relaxation is used with the 4th order accuracy viscous scheme and the 5th WENO scheme with an improved ε value of 10^{-2} to achieve steady state solutions with high convergence rate and level.

The following cases are calculated to demonstrate the high order methodology developed: 1) 1D unsteady Sod shock tube; 2) The 1D unsteady Shu-Osher Problem with a Mach 3 shock wave interacting with a sine entropy wave. 3) a flat plate supersonic laminar boundary layer; 4) a subsonic flat plate turbulent flow solution with Baldwin-Lomax turbulent model; 5) an inviscid 2D converging-diverging nozzle with oblique shock waves and reflections; 6) the transonic flow over RAE2822 airfoil.

Numerical results show that the methodology is efficient and robust.

5   Acknowledgment

References

[1] X.D.Liu, S.Osher, and T.Chan, "Weighted essentially non-oscillatory schemes," *J.Comput.Phys.*, vol. 126, pp. 200–212, 1994.

[2] G.S.Jiang, and C.W.Shu, "Efficient implementation of weighted ENO schemes," *J.Comput.Phys.*, vol. 126, pp. 202–228, 1996.

[3] V.A.Titarev, E.F.Toro, "Finite-volume WENO schemes for three-dimensional conservation laws," *J.Comput.Phys.*, vol. 201, pp. 238–260, 2004.

[4] T.Zhou, Y.Li, C.W.Shu, "Numerical comparison of WENO finite volume and Runge-Kutta discontinuous Galerkin methods," *J.Sci.Comput.*, vol. 16, pp. 145–171, 2001.

[5] M.Latini, O.Schilling, W.S.Don, "Effects of WENO flux reconstruction order and spatial resolution on reshocked two-dimensional Richtmyer-Meshkov instability." J. Comput. Phys., 2006, doi:10.1016/j.jcp.2006.06.051, 2006.

[6] Nelida Crnjaric-Zic, Senka Vukovic, Luka Sopta, "Balanced finite volume WENO and central WENO schemes for the shallow water and the open-channel flow equations," *J.Comput.Phys.*, vol. 200, pp. 512–548, 2004.

[7] A.Beaza, P.Mulet, "Adaptive mesh refinement techniques for high-order shock capturing schemes for multi-dimensional hydrodynamic simulations," *International Journal for Numerical Methods in Fluids*, vol. 52, pp. 455–471, 2006.

[8] B.Sjogreen and H.C.Yee, " Low dissipative high-order numerical simulations of supersonic reactive flows," *International Journal for Numerical Methods in Fluids*, vol. 43, pp. 1221–1238, 2003.

[9] C.-W. Shu, "Essentially Non-Oscillatory and Weighted Essentially Schemesfor Hyperbolic Conservation Laws." NASA/CR-97-206253, 1997.

[10] B. Van Leer, "Towards the Ultimate Conservative Difference Scheme, III," *Journal of Computational Physics*, vol. 23, pp. 263–75, 1977.

[11] Y.N.Chen, S.C.Yang, and J.Y.Yang, "Implicit weighted essentially non-oscillatory schemes for the incompressible Navier-Stokes equations ," *International Journal for Numerical Methods in Fluids*, vol. 31, pp. 747–765, 1999.

[12] J.Yang, Y.Perng, R.Yen, "Implicit weighted essentially nonoscillatory schemes for the compressible Navier-Stokes equations," *AIAA J.*, vol. 39, pp. 2082–2090, 2001.

[13] A.Cadiou, and C.Tenaud, "Implicit WENO shock capturing scheme for unsteady flows. Application to one-dimensional Euler equations," *International Journal for Numerical Methods in Fluids*, vol. 45, pp. 197–229, 2004.

[14] L.Yuan, "Comparison of implicit multigrid schemes for three-dimensional incompressible flows," *J. Compu. Phys.*, vol. 177, pp. 134–155, 2002.

[15] Y.Q. Shen, B.Y.Wang,and G.C.Zha, "Comparison Study of Implicit Gauss-Seidel Line Iteration Method for Transonic Flows." AIAA-paper 2007-4332, Jun. 2007.

[16] P. Roe, "Approximate Riemann Solvers, Parameter Vectors, and Difference Schemes," *Journal of Computational Physics*, vol. 43, pp. 357–372, 1981.

[17] C.-W. Shu and O. Osher, "Efficient Implementation of Essentially Non-Oscillatory Shock Capturing Schemes," *Journal of Computational Physics*, vol. 77, pp. 439–471, 1988.

[18] M. L. Mason and L. E. Putnam, "The Effect of Throat Contouring on Two-Dimensional Converging-Diverging Nozzles at Static Conditions ." NASA Technical Paper 1704, 1980.
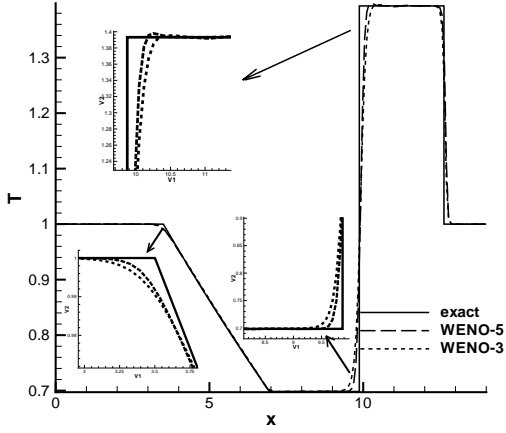
Figure 2: Temperature distribution of Sod's problem
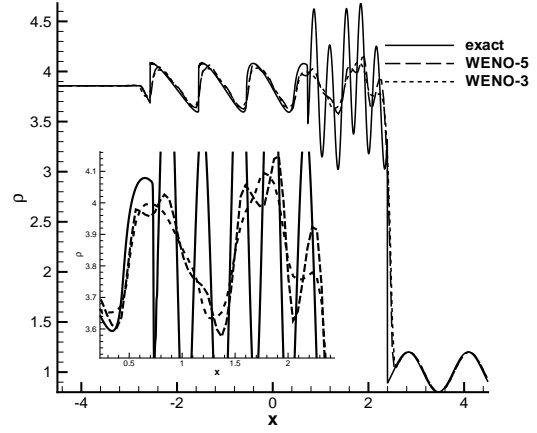
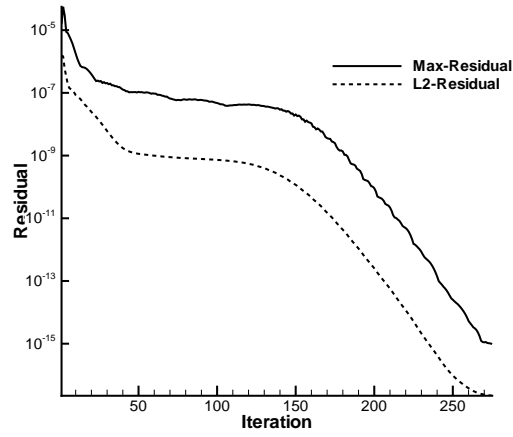Figure 3: Density distribution of Shu-Osher's problem

Figure 4: Convergence rate of the supersonic boundary layer flow using WENO-5
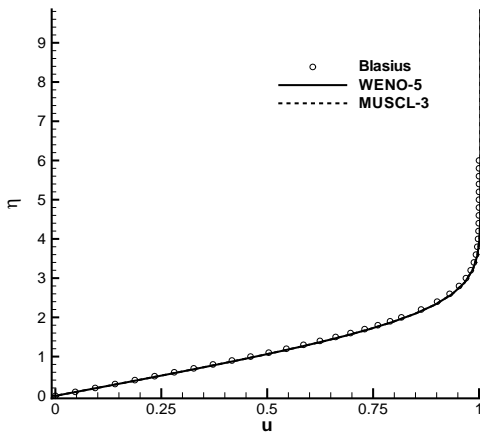

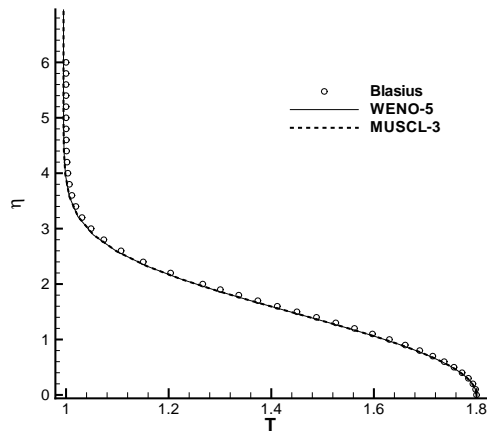Figure 5: Velocity profile of the supersonic boundary layer flow

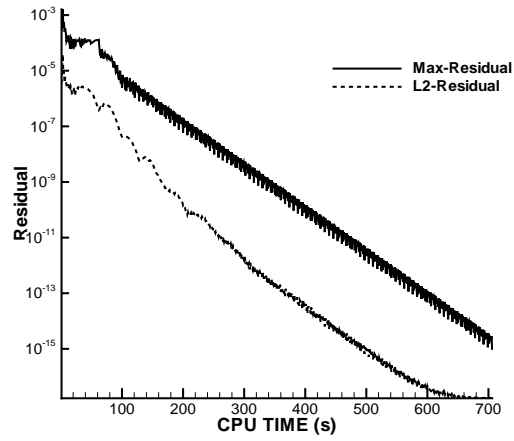Figure 6: Temperature profile of the supersonic boundary layer flow

13

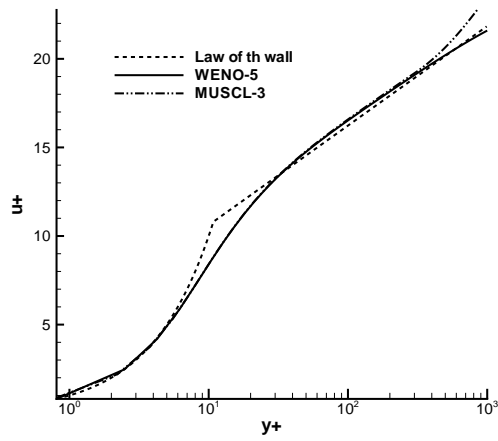Figure 7: Convergence rate of subsonic flat plate turbulent boundary layer by using WENO-5
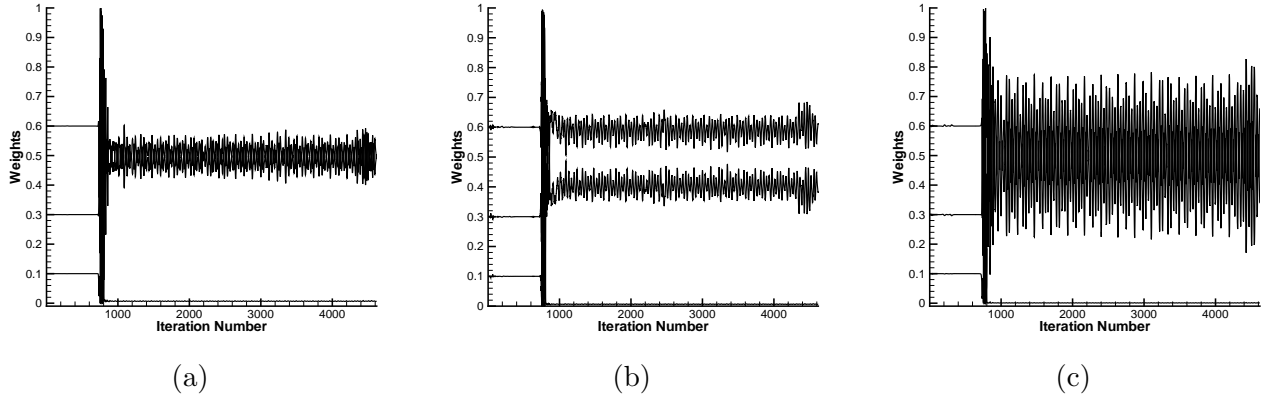

Figure 8: Velocity profile of turbulent boundary layer

14

Figure 9: The variations of weights vs iteration number in ξ-direction at the point $(8.315, 1.117)$, the transonic converging-diverging nozzle flow, $\varepsilon = 10^{-6}$. (a): $\rho^L_{i+1/2}$, (b): $(\rho u)^L_{i+1/2}$, (c): $(\rho v)^L_{i+1/2}$.
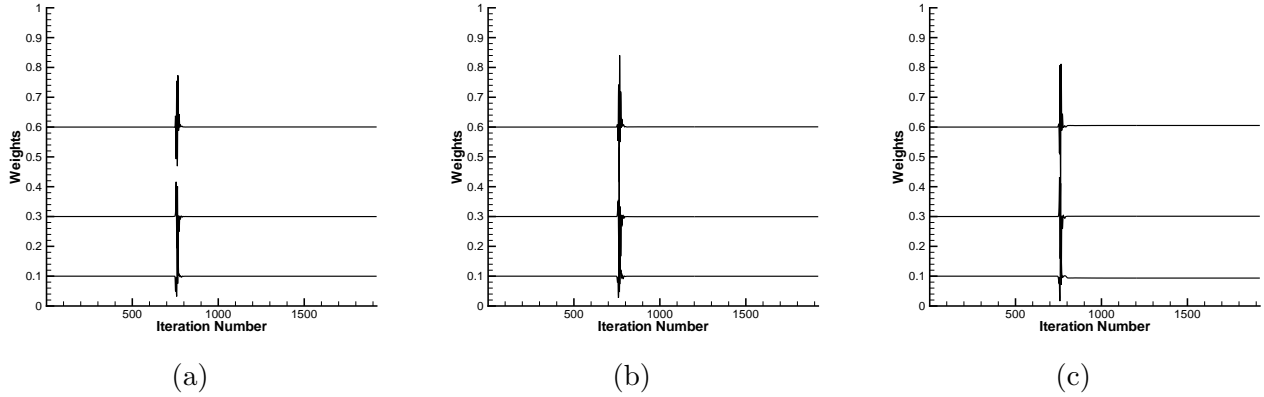
Figure 10: The variations of weights vs iteration number in ξ-direction at the point $(8.315, 1.117)$, the transonic converging-diverging nozzle flow, $\varepsilon = 10^{-2}$. (a): $\rho^L_{i+1/2}$, (b): $(\rho u)^L_{i+1/2}$, (c): $(\rho v)^L_{i+1/2}$.
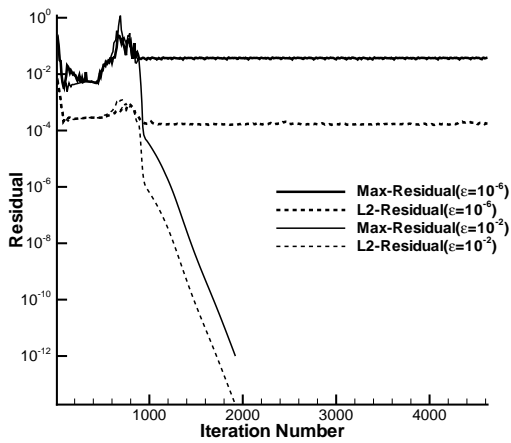
Figure 11: Convergence rate of the transonic converging-diverging nozzle flow

Figure 12: Comparison of the pressure coefficients at the upper wall of the transonic converging-diverging nozzle flow
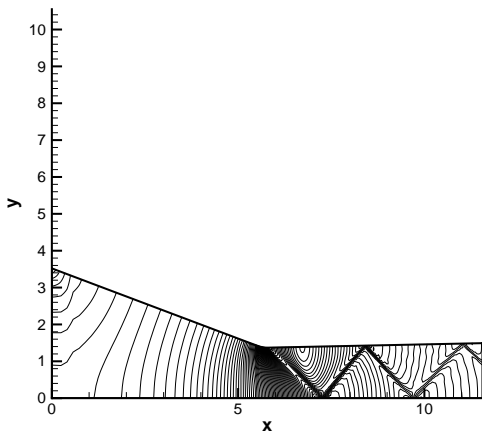
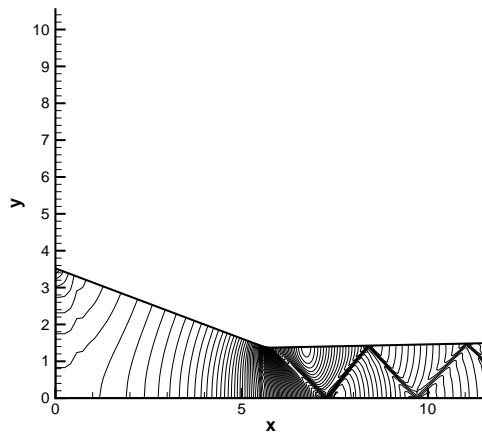Figure 13: Pressure contours of the transonic converging-diverging nozzle flow, $\varepsilon = 10^{-6}$

Figure 14: Pressure contours of the transonic converging-diverging nozzle flow, $\varepsilon = 10^{-2}$
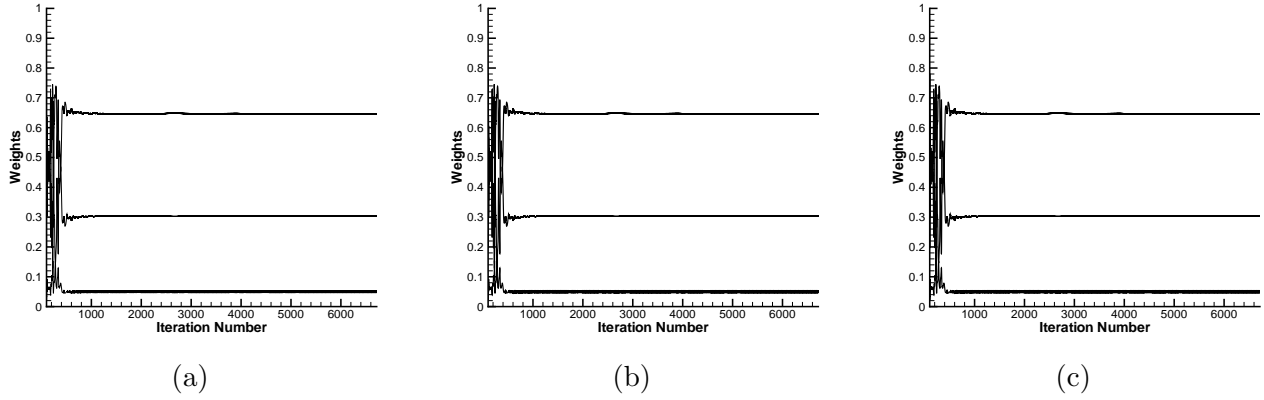
(a)   (b)   (c)

Figure 15: The variations of weights vs iteration number in η-direction at the point $(0.209, 0.066)$, the transonic flow over RAE2822 airfoil, $\varepsilon = 10^{-6}$. (a): $\rho_{j+1/2}^L$, (b): $(\rho u)_{j+1/2}^L$, (c): $(\rho v)_{j+1/2}^L$.
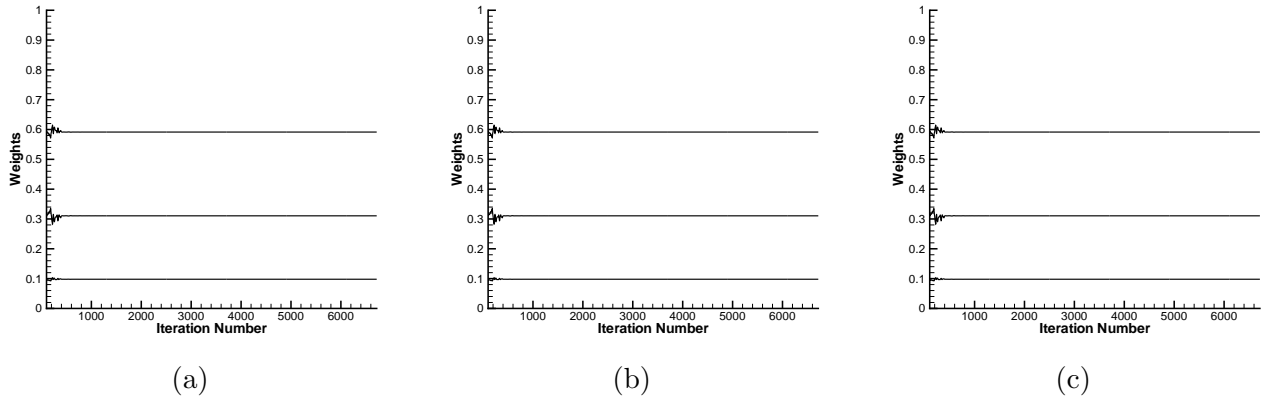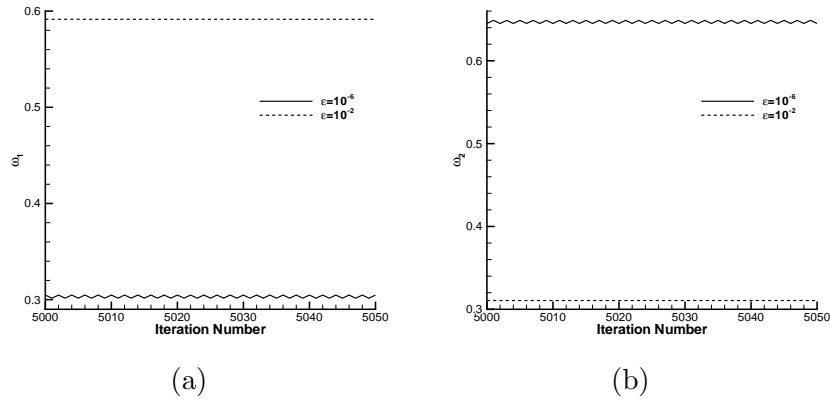

(a)   (b)   (c)

Figure 16: The variations of weights vs iteration number in η-direction at the point $(0.209, 0.066)$, the transonic flow over RAE2822 airfoil, $\varepsilon = 10^{-2}$. (a): $\rho_{j+1/2}^L$, (b): $(\rho u)_{j+1/2}^L$, (c): $(\rho v)_{j+1/2}^L$.

(a)   (b)

Figure 17: The comparisons of weights η-direction at the point $(0.209, 0.066)$, the transonic flow over RAE2822 airfoil. (a): ω_1, (b): ω_2.
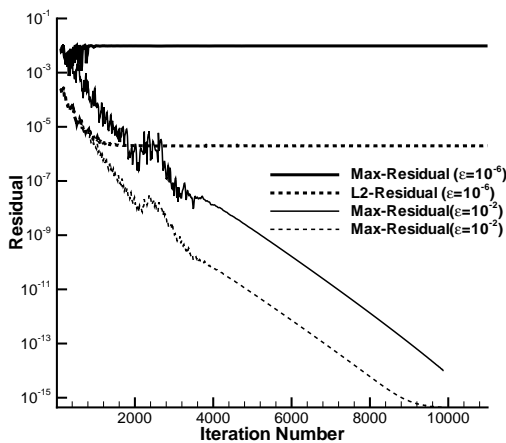
17

Figure 19: Comparison of the pressure coeffi-

Figure 18: Convergence rate of the transonic cients at the airfoil surface of the transonic flow
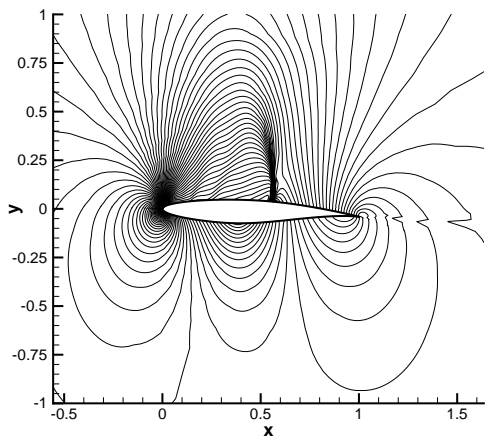flow over RAE2822 airfoil over RAE2822 airfoil

Figure 20: Pressure contours of the transonic
flow over RAE2822 airfoil , $\varepsilon = 10^{-6}$